

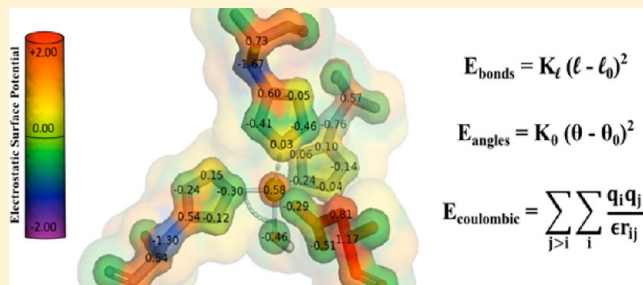
Parameters for Molecular Dynamics Simulations of Manganese-Containing Metalloproteins

Rui P. P. Neves, Sérgio F. Sousa, Pedro A. Fernandes, and Maria J. Ramos*

REQUIMTE, Departamento de Química e Bioquímica, Faculdade de Ciências, Universidade do Porto, Rua do Campo Alegre, s/n, 4169-007 Porto, Portugal

S Supporting Information

ABSTRACT: A set of geometrical parameters has been determined for single manganese metalloproteins for the AMBER force field, and ultimately to other force fields with a similar philosophy. Twelve (12) models from 9 different single-cluster manganese proteins were optimized and parametrized, using a bonded model approach. Mn-ligand bonds, Mn-ligand angles, and Restrained Electrostatic Potential charges for all the 74 residues in the first metal coordination sphere of each Mn metalloprotein were parametrized. The determined parameters were validated with molecular dynamics simulations and several statistics strategies were used to analyze the results. In addition, to validate the parametrized models, frequency and normal mode calculations were performed and comparisons were obtained for the overall structures both with quantum mechanics and molecular mechanics calculations. Linear and polynomial fittings were performed to estimate Mn-ligand bond force constants for generic manganese centers. Furthermore, averages are proposed for the main Mn-ligand angle interactions of typical manganese coordination centers: axial, square and triangular equatorial planes, and tetrahedral positions, for the different combinations of donor atoms from waters and hard ligands.



INTRODUCTION

Biomolecular force fields are very important tools in current computational chemistry and biochemistry, because they allow a large sampling of the phase space of biological systems and their respective studies at an atomistic level.

Among the fundamental units of biochemistry, biological systems have ions and ligands that participate in the function or organization of these systems. In current biomolecular force fields, all units are described by a set of constant parameters. In particular, metalloproteins represent a challenge in the field due to the complex behavior of inorganic cofactors and transition-metal ions.^{1–4} This translates in large difficulties to introduce general criteria for these systems and in the lack of available parameters.

Following this premise, a search for a unified force field for metal biological systems is a contemporary matter, given its current importance not only in biochemical systems but also for the nanotechnology and pharmaceutical industries.^{5–7}

Manganese is one of the more frequent metals that figure in the available crystallographic files in the Protein Data Bank.^{6,8} A search, both in the Protein Data Bank⁹ and in the literature,^{10–12} on manganese metalloproteins, shows that the main donor atoms to this metal are oxygen (from carboxylate or main carbonyl groups) and nitrogen (from imidazole rings).⁶

Manganese is found in all six classes of enzymes.^{6,10} Computational studies have been conducted on the redox properties of manganese systems, such as the superoxide

dismutase and the photosystem II or manganese catalases and peroxidases.^{6,12,13} These systems are found to be relevant in water oxidation or oxygen synthesis.^{10,11}

Manganese is known to be generally 5- or 6-coordinated, although a typical coordination number is not defined in the literature.^{10,11} Therefore, its geometries are usually derived from an octahedron. Manganese is usually in the Mn(II) oxidation state. However, in manganese clustered systems, it can be found in combinations of Mn(III)/Mn(IV) or Mn(II)/Mn(IV) and is generally involved in electron transport chains.¹¹

Manganese-coordinated systems are described as high-spin complexes. This characteristic generally leads to a high-spin multiplicity in the metal center and weak ligand fields.¹² The high-spin multiplicity also allows one to collect atomistic-level, higher-resolution data since Mn ions ensure high EPR signals.^{10,14} As a result, Mn can be soaked in protein crystals or co-crystallized with metalloprotein, in place of magnesium, calcium, or zinc, which have no EPR signal response.¹⁴ Moreover, Mn can exchange easily with Zn or Mg even in crystallized proteins.¹⁰

Several approaches have been described for the parametrization of metalloproteins,^{3,15} all of them having their own limitations. Among the most commonly cited, there are the nonbonded,¹⁶ the cationic dummy atom,¹⁷ and the bonded

Received: January 22, 2013

Table 1. List of Parameterized Manganese Enzymes[†]

Name	PDB code	Model code	Resolution	Geometry	Spin multiplicity	Global charge
Superoxide Dismutase (resting state)	1N0J ⁴⁰	HHDHW (III)	2.20		5	+2
Superoxide Dismutase ^(a) (resting state)	1N0J ⁴⁰	HHDH[HO] (III)	2.20		5	+1
Superoxide Dismutase ^(b) (enzyme-substrate complex)	1MNG ⁴¹	HHDH[HO]O (III)	1.80		4	0
Cytochrome C Oxidase	3HB3 ⁴²	HDEWW (II)	2.25		6	0
D-Glutarate Dehydratase ^(c)	3NXL ⁴³	DENWW (II)	1.89		6	0
Integrase	1A5V ⁴⁴	DDWWW (II)	1.90		6	0
Muconate Cycloisomerase ^(c)	3CT2 ⁴⁵	DEDWW (II)	1.80		6	-1
Pyruvate Kinase	2G50 ⁴⁶	ED[PY2]WW (II)	1.65		6	-1
Homoprotocatechuate 2,3-dioxygenase	1F1U ⁴⁷	HHEWW (II)	1.50		6	+1
Mandelate racemase ^(d)	2MNR ⁴⁸	DEE[SO2] (II)	1.90		6	-3
Pneumococcal Surface Antigen Adhesin A ^(c)	1PSZ ⁴⁹	HHE[D2] (II)	2.00		6	0
Chloromuconate cycloisomerase	2CHR ⁵⁰	DED[CL] (II)	3.00		6	-2

[†]The first three models concern the superoxide dismutase system; then, the systems are organized by decreasing coordination number and in alphabetical order. Specific codes were attributed to each model, according to the identity of its ligands. The symbols H, D, E, and N represent the one-letter amino acid code of histidine, aspartate, glutamate and glutamine, respectively. The symbols W, HO, O, PY, SO, CL represent the waters, hydroxides, superoxides, pyruvates, sulfates and chloride, respectively. Bidentate ligands are identified by the number 2, which is associated with the codes specified above. The oxidation state is identified by the roman numeral suffix given at the end of the model code. ^(a)The water ligand suggested from the crystallographic structure was treated as a hydroxide. ^(b)The azide ligand, considered as a superoxide analogue,⁵¹ was rebuilt as a superoxide ion. ^(c)3NXL and 3CT2 were obtained from crystallized structures complexed with Mg²⁺ as metal center and 1PSZ was complexed with Zn²⁺. For the calculations performed here, these ions were replaced by Mn²⁺, attending to Mn²⁺ exchangeability with these ions. ^(d)Coordinated waters suggested by the crystallographic structure were removed, attending to the reviewed literature.¹⁰

model approaches.¹⁸ The latter is the most complete in what concerns the description of the internal coordinates associated to the metal coordination center.

The use of the nonbonded or cationic dummy atom approaches has been shown to be ineffective when dealing with several metalloproteins,^{2,3,19–21} leading often to significant geometrical distortions and ligand exchange, unrealistic from a biological point of view. Bonded model approaches, although more computationally and time demanding, introduce classical mechanical parameters. In this model, metal–ligand stretching and bending modes are described by molecular mechanical potentials.¹⁸ The flipside is that, in several biological systems, coordination spheres change, especially when considering weak ligand fields, and the process is limited by this approach. Even so, bonded model approaches have allowed studies of the interactions between ligands and the metal ion centers to be made,^{22–27} as well as ensuring a good structural description of the protein.

Parameters in a force field for biologically relevant metallo-centers must reproduce the geometrical properties of their

coordination sphere, typical metal–ligand modes, and charge density.^{15,28} An all-atom approach is used the most in most common force fields,^{29–34} describing bond and angle interactions with harmonic potentials and intermolecular interactions (for atoms separated by more than 3 bonds, using electrostatic and dispersion terms). In addition, torsion sinusoidal terms can be added using Fourier expansions and improper constraints can be taken into account, described as harmonic potentials between coplanar nonconcurrent bonds.^{15,28,35} The terms that highly influence the specificity of the coordination sphere and nature of the metal, thus needing accurate description, are bond stretching and angle bending modes, and electrostatics.^{18,36}

In the proposed parametrization scheme, we chose to parametrize single Mn coordination spheres with a bonded model approach.

Ultimately, correlations between the calculated parameters and their coordination spheres can be established. We will focus on properties such as sphere geometry or ligand position/combination. Such, we expect, will allow some level of

transferability of the bonded-model parameters determined, for other Mn metalloproteins or force fields, not directly evaluated in this study.

■ COMPUTATIONAL DETAILS

The parametrization scheme proposed follows from the AMBER²⁹ force-field potential formalism. The potential energy determined from the force-field equation is a function of the Cartesian coordinates of each atom, from which are calculated bond stretching, angle bending, torsional variables, and atomic distances. The remaining terms in the equation are parameters that must be determined either from theoretical or experimental means:

$$U(\vec{r}) = \sum_l K_l (l - l_0)^2 + \sum_\theta K_\theta (\theta - \theta_0)^2 + \sum_\rho K_\rho [1 + \cos(n\rho - \gamma)] + \sum_{j>i} \sum_i \left\{ \epsilon_{ij} \left[\left(\frac{R_{ij}}{r_{ij}} \right)^{12} - \left(\frac{R_{ij}}{r_{ij}} \right)^6 \right] + \frac{q_i q_j}{\epsilon r_{ij}} \right\}$$

In the proposed scheme bond and angle parameters, K_l and K_θ , and equilibrium values, l_0 , and θ_0 , are determined from linear transit scan along the internal coordinates associated with metal–ligand interactions. Electrostatic charges (q_i) are determined from a RESP fitting of Merz–Kollman charges.

Dihedral force constants (K_ρ) involving the metal ion are set to zero, while transferable van der Waals atomic parameters are taken from the literature.^{36–39}

Building Parametrizable Models. We listed all relevant Mn metalloproteins,^{10,11} defined their coordination spheres, and selected the adequate crystallographic structures of those macromolecules.

From the benched manganese proteins, a set of single manganese proteins was chosen to build models smaller than 100 atoms. Table 1 lists the 12 parametrized models from the crystallographic structures.

The initial models were obtained from the initial crystallographic structures by selecting only the Mn ion and the residues bonded to it. Note that this process involved a set of assumptions, as the coordination shell of Mn in some of the structures could not be unequivocally assigned.^{10,52,53} Coordinated water molecules are many times unresolved in the X-ray structures and sometimes they exceed the maximum number of coordination that Mn allows for (six). Literature points toward 1–3 waters coordinated in Cytochrome C Oxidase,⁵⁴ even though all structures analyzed possess exactly three water molecules. In pyruvate kinase, studies refer to the existence of one water molecule,⁵⁵ but the structures that we have analyzed always have two. In the structure from Mandelate Racemase, we observed two waters within a 2 Å distance from the Mn ion, even though they were not mentioned in the literature.¹⁰

To determine the force-field parameters defined above, the 12 models built from the crystallographic structures were optimized at the B3LYP/SDD:6-31G(d,p) level of theory using the Gaussian09 package.⁵⁶ B3LYP^{57–59} is currently the most used functional, yielding good results in the estimate of several thermodynamic quantities^{60,61} and the use of the effective core potentials (ECPs) is a common feature in the optimization of systems with transition metals.^{22,62,63} On the latter, the

SDD,^{64,65} implemented in the Gaussian software, has been widely used in several studies.^{7,21,22,37,66–69}

The initial model was relaxed using a semiflexible model approach. In this approach, the backbone atoms (α -carbon, terminal nitrogen atom and carbonyl group) of the bonded amino acids were frozen during the optimization. In Figure 1, we present a scheme on the restraints imposed to the metalcenter built from the crystallographic structures approached.

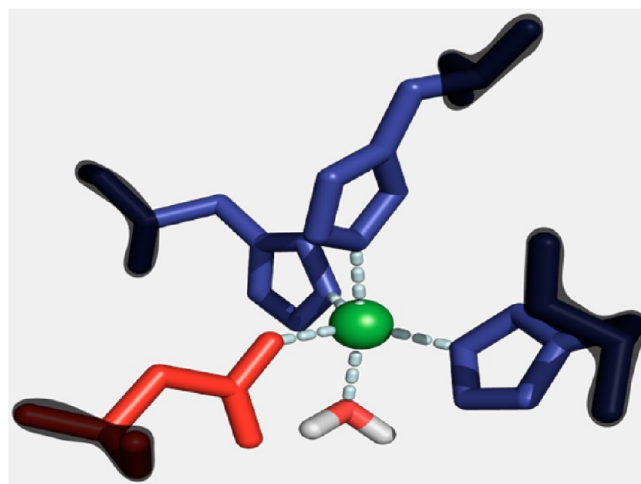


Figure 1. Scheme on the semiflexible approach took toward the study of manganese metalcenters. The grayish area delimits the atoms that were frozen during the geometry optimization (α -carbon, terminal nitrogen atom, and carbonyl group).

In the treatment of ligands such as sulfates, we have protonated distant basic groups. With this procedure, we intended to avoid artifacts such as deprotonations or the establishment of unexpected hydrogen bonds, because of the lack of environment. Some atoms further from the metal center were frozen in order to avoid large changes in geometry relative to the initial crystallographic structure, ensuring a correct description of the chemistry of the enzyme by the model.

From the geometry optimizations performed at the quantum level, for the 12 initial models considered, a good agreement was observed between the literature predictions,^{6,8,12} the X-ray structures, and the computational optimization.

Figure 2 shows the initial optimized structures: six of the models are 6-coordinated, presenting distorted octahedral geometries; four models are 5-coordinated, four present a distorted bipyramidal trigonal geometry, and two exhibit a distorted quadrangular pyramidal geometry; the remaining model is (4)-coordinated, exhibiting distorted tetrahedral geometry.

In the model HHE[D2], we observed an asymmetrical bonding of the aspartate residue in a bidentate way. This model was built substituting the Zn ion for a Mn²⁺ ion, as suggested from the literature.^{10,49}

Bond and Angle Parameters. In order to determine bond and angle equilibrium values to all bonds with the metal ion, a different semiflexible approach was used, as described in Figure 3. Optimizations prior to the determination of the potential energy surface (PES) were performed by freezing the nonscanned ligands and the backbone of scanned ligands, at the B3LYP/SDD:6-31G(d,p) level of theory.

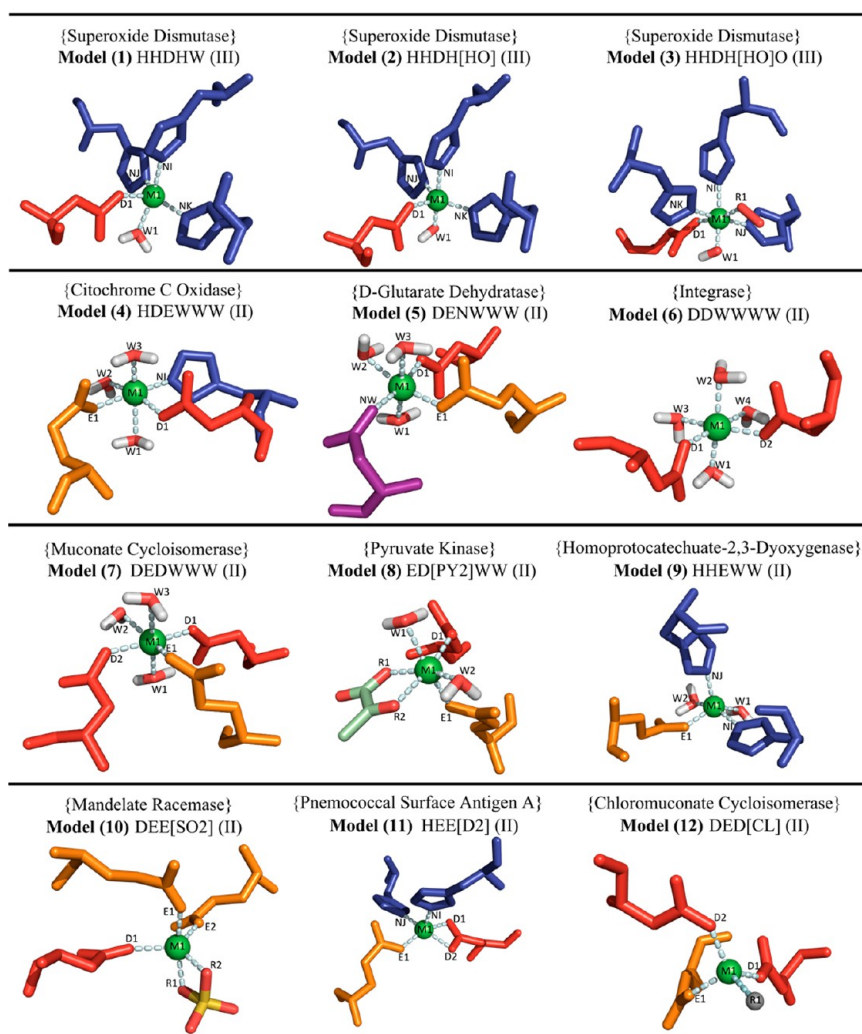


Figure 2. Representation of the 12 models parametrized in the presented study. The main residues are colored blue, red, orange, purple, and green for histidines, aspartates, glutamates, asparagines, and the manganese center, respectively. Hydrogen, carbon, and oxygen atoms are colored white, pale green, and red, respectively.

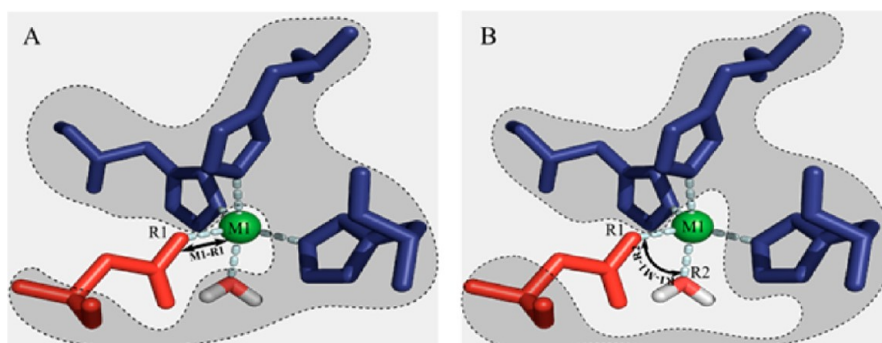


Figure 3. (A) Bond scan procedure and (B) angle scan procedure. In both figures, the darker areas delimit the set of atoms frozen during the optimization prior to the PES determination and in the PES determination.

Figure 3 also illustrates the semiflexible approach scheme used to determine the PES for each of the parametrized Mn-ligand bond and angle coordinates. In this approach, we freeze all degrees of freedom except the one being parametrized, to be consistent with the independence of all terms in the force field equation.

The PES scans were performed with a range of 30 increments for both sideways of the PES minima, resulting in

a total metric range of 0.12 Å and 30° around the PES minima. Bond and angle force constants were determined from the best fitting to the harmonic potential approximation.

All angles involving the metal ion as a terminal atom were determined using the same methodology with 20 increment steps, approaching 20° around the PES minima.

Atomic Single Charges. Atomic point charges were calculated using the Restrained Electrostatic Potential (RESP)

methodology,⁷⁰ considering the Coulomb potential for the calculation of electrostatic interactions.

The standard AMBER force fields are parametrized at a HF/6-31G(d) level of theory.²⁹ The standard procedure often underestimates the effects of charge transfer with the metal atom,^{71,72} therefore, density functional theory (DFT) is considered to be a more successful approach to calculate RESP charges.^{36,37,39,73,74} Atomic charges were calculated on the optimized structures, at the B3LYP/6-311++G(3df,3pd) level of theory. A default Merz–Kollman radii of 2.00 Å was assigned to the metal center.⁷⁵ Charges for the carbonyl and nitrogen of the amine, from the backbone of the ligands, were fixed according to the parameters established by Cornell et al.²⁹

van der Waals Parameters. van der Waals interactions are considered transferable. Therefore, the van der Waals (vdW) parameters were transferred from the PARM99⁷⁶ force field of the AMBER package (parameters for the water hydrogen were considered equivalent to those in hydrogen sulfide).

The van der Waals (vdW) parameters of the Mn ions were transferred from the works of Babu et al.,⁷⁷ on the determination of vdW parameters from the hydration free energies of hydrated divalent-metal cation shells.

Dihedral Parameters. The force constants concerning torsional movements were set to zero, because it is a standard procedure in the parametrization of metal centers.^{18,37,71,78} In fact, unless there is π -delocalization, this assumption has been verified both experimentally and theoretically.⁷⁹ This consideration simplifies the systems' parametrization approach, because the number of dihedrals in a coordination sphere is higher than the number of bonds or metal-centered angles.

Validation Procedure. To check how well the Molecular Mechanics (MM) parameters reproduced the geometric properties of the Quantum Mechanics (QM) systems, we reoptimized the latter at the MM level and compared the MM and QM geometries. We have also compared the MM and QM vibrational frequencies.

In addition, we checked if the MM parameters could reproduce the geometries of the Mn center within an enzymatic scaffold. For that purpose, we run 12 molecular dynamics (MD) simulations of nine different metalloenzymes containing manganese. MD simulations were performed using the AMBER10 package.⁸⁰

Letter and number codes were established to label the residues parametrized (three-letter code) and the bonding atoms (two-letter code). The labeling criteria of parametrized residues and coordinating atoms is presented in the Supporting Information.

For each of the 12 biological systems studied, we built models from the crystallographic structure of the protein, constituted by at least one monomer of the unit, to validate the parameters determined. The mechanical parameters of the organic ligands coordinated to the metal center were parametrized using the ANTECHAMBER module⁸¹ of AMBER10, with the GAFF force field.⁸² All remaining ligands and co-factors not included in the coordination sphere under study were removed from the initial crystallographic structures.

We added counterions to the system in order to neutralize its global charge and created a rectangular solvent box with TIP3P waters,⁸³ so that the distance between the protein and the edges of the box was set to 12 Å. This value fits the average conditions commonly used in several other studies with a same prospect,^{36,37,74} since the *cutoff* for the discrete account of vdW interactions is generally within the range of 9–15 Å.⁸⁴

For the built systems, 10 ns of MD were performed, preceded by a four-step minimization, to minimize waters, added hydrogens, residue side chains, and all the atoms of the system. An equilibration step of 40 ps was applied, in order to gradually heat the temperature of the system to the standard temperature of 310 K, at a constant pressure of 1 bar. MD proceeded on a NPT ensemble. A constant temperature of 310 K was maintained by the use of Langevin Dynamics implemented in AMBER10 package and a fixed pressure of 1 bar was set. Periodic boundary conditions were imposed to the models built to account for long-range interactions. Short and long-range interactions were calculated with Ewald summation methods.⁸⁵ The SHAKE algorithm⁸⁶ was applied in all bonds involving hydrogen atoms, for a mechanical relaxation time of 2 ps. To calculate long-range vdW interactions, a *cutoff* distance of 10 Å was established.

Different scaling factors for the 1–4 electrostatic interactions were tested, resulting in a final scaling factor of 60% in all MM calculations, applying the parameters determined.

MD results were obtained with the PTRAJ module of the AMBER package. Values analyzed included the root-mean-square deviations (RMSDs) for the α -carbons of all the models, and for all the atoms in the metal coordination sphere. Average and standard deviation values for all the bonds and angle involving the metal atoms were taken from the final 4 ns of MD simulations.

RESULTS AND DISCUSSION

Bond Stretching Parameters. From a total of 64 bond force constants determined, 14 of them characterize Mn–N bonds and the other 50 characterize Mn–O bonds.

Figure 4 illustrates the PES obtained for all of the Mn–ligand bond scans.

All the equilibrium bond lengths are found in the interval]2.00; 2.45[Å in all systems. However, for smaller charged ligands, this value can be smaller, as seen in the models with the hydroxide ion. For the studied amplitude in bond stretching energetics, increments below 0.5000 kcal mol^{−1} are frequent. Most of the force constants are in the 60–80 kcal mol^{−1} Å^{−2} range.

We can observe similarities in the PES when the equilibrium bond lengths are ~2.15–2.20 Å for nitrogen donor atoms, and ~2.10 and ~2.30 Å for nonwater and water oxygen donor atoms, respectively. These observations are in qualitative agreement with the general knowledge regarding transition-metal chemistry and the expected relative magnitude of the corresponding force constants.^{6,12}

For similar bond lengths, histidines exhibit higher force constants than glutamates or aspartates. Waters are the weakest ligands, with larger typical bond lengths and shallower PESs.

It is important to highlight, because of the large amount of information in literature concerning the manganese superoxide dismutase,^{12,51,52,87} some relevant discussion from the determined parameters. Conformational changes between the two models of manganese superoxide dismutase occur mainly in the axial ligands, when the hydroxide ligand is present instead of the water ligand. As the hydroxide ligand deepens into the coordination sphere, we observe that the axial histidine approaches the metal center and its force constant increases. By bonding with the superoxide substrate, the model becomes 6-coordinated with distorted octahedral symmetry and exhibits a Jahn–Teller effect along the NI–W1 axis, as described in the literature.¹²

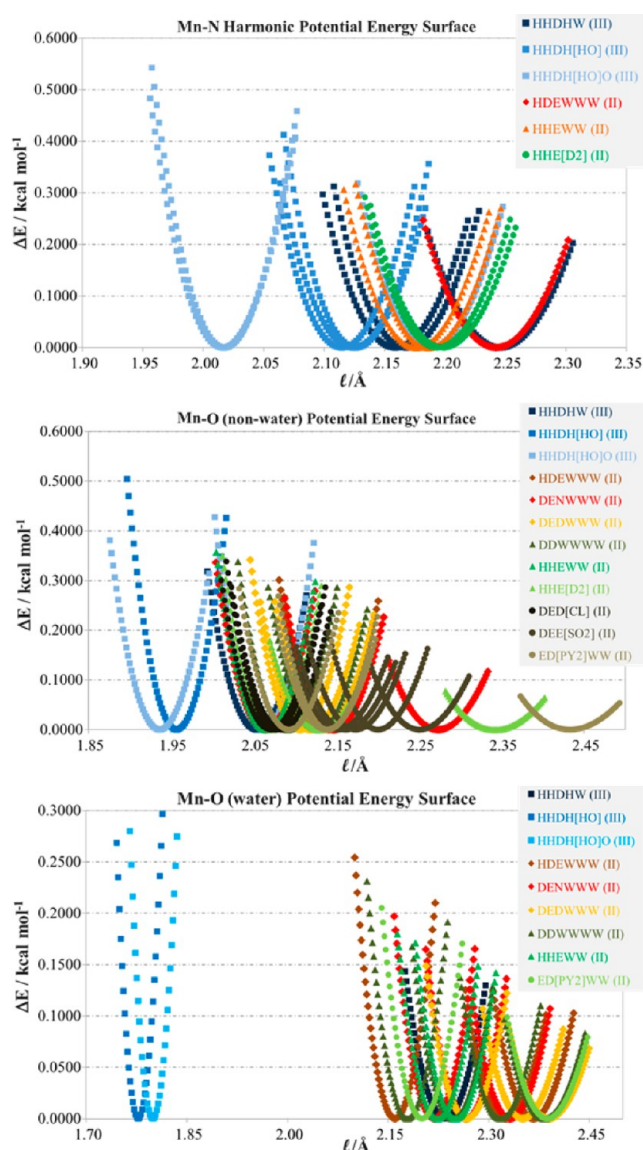


Figure 4. Potential energy surfaces (PESs) for bond stretching for all models.

The analysis of the internal bonding terms also suggests that similar coordination spheres do not differ substantially either in bond length or bond force constant.

Angle Bending Parameters. From the total parametrized 146 metal-centered bond angles (the detailed full set of parametrized metal-centered angles is provided in the Supporting Information) their distribution is as follows: 11 for N–Mn–N, 22 for N–Mn–O, 16 for N–Mn–water, 31 for O–Mn–O, 46 for O–Mn–water, and 17 for water–Mn–water (in this distribution, hydroxides have been counted together with waters).

Analysis of Figure 5 shows that angle force constants are often $<75 \text{ kcal mol}^{-1} \text{ rad}^{-2}$. The cases in which this is not verified mainly concern interactions with histidines.

The bidentate ligands studied exhibit force constants of $>100 \text{ kcal mol}^{-1} \text{ rad}^{-2}$, and $>200 \text{ kcal mol}^{-1} \text{ rad}^{-2}$ for the bidentate ligands whose donor atoms are bonded to the same atom.

For 6-coordinated models, interaction between nonwater donor atoms and water oxygen atoms is frequent, establishing mainly orthogonal interactions with force constants abundantly

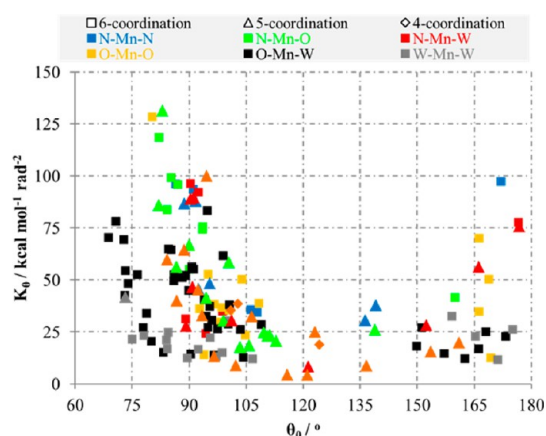


Figure 5. Angle force constants and equilibrium angles from the scan of the studied models, by donor atom type and coordination number.

between 25 and $75 \text{ kcal mol}^{-1} \text{ rad}^{-2}$. In the axial positions, the force constants are $\sim 25 \text{ kcal mol}^{-1} \text{ rad}^{-2}$.

Regarding the 5-coordinated complexes, two possible geometries are observed: bipyramidal trigonal and square pyramidal. In the triangular equatorial plane, interactions with nitrogen donor atoms are more frequent and with low force constants ($<25 \text{ kcal mol}^{-1} \text{ rad}^{-2}$), while for the axial positions, they are generally near $25 \text{ kcal mol}^{-1} \text{ rad}^{-2}$. In square pyramidal geometries, most interactions are observed from histidines with force constants slightly below the $25 \text{ kcal mol}^{-1} \text{ rad}^{-2}$.

The 4-coordinated model has a distorted tetrahedral geometry with force constants slightly above the $25 \text{ kcal mol}^{-1} \text{ rad}^{-2}$ for angles of $\sim 109.5^\circ$.

Analyzing the angle force constants, we can conclude that their amplitude is not strongly concerned with the geometrical position of the ligands for the equilibrium bending amplitudes frequently observed, despite some geometrical similarities observed in models (4)–(7) (recall Figure 2). Looking further into the donor atom type, it seems that oxygen donor atoms from aspartates and glutamates establish stronger angle bending interactions with waters than N atoms from histidines, when in equatorial positions; however, for orthogonal interactions with axial waters, higher angle force constants are generally observed with histidine ligands.

RESP Charges Calculation. Single-point electrostatic potentials were calculated using the large 6-311++G(3df,3dp) basis set.

Figure 6 shows the charge schemes for the donating groups of the ligands in the models from manganese superoxide dismutase (models (1)–(3)), and the global charge of each residue from their coordination sphere (a detailed description of the RESP charge maps for the 12 metalcenters parametrized is presented in Supporting Information).

Overall, RESP atomic charges were determined for 74 residues, in the 12 models used for parametrization.

As we can see in a dispersion pattern for manganese and its main biological ligands, in Figure 7, there is a large dispersion in the global charges of the residues, mainly on the Mn ion. That might concern the fact that the Mn ion is buried within the coordination sphere by its ligands, which is a consequence from the ESP methodologies extensively described in the literature.^{75,88} An average estimate seems to agree with the classical expected zero charge only for waters.

Parameter Validation. A validation protocol was designed to verify the stability of the protein backbone and the

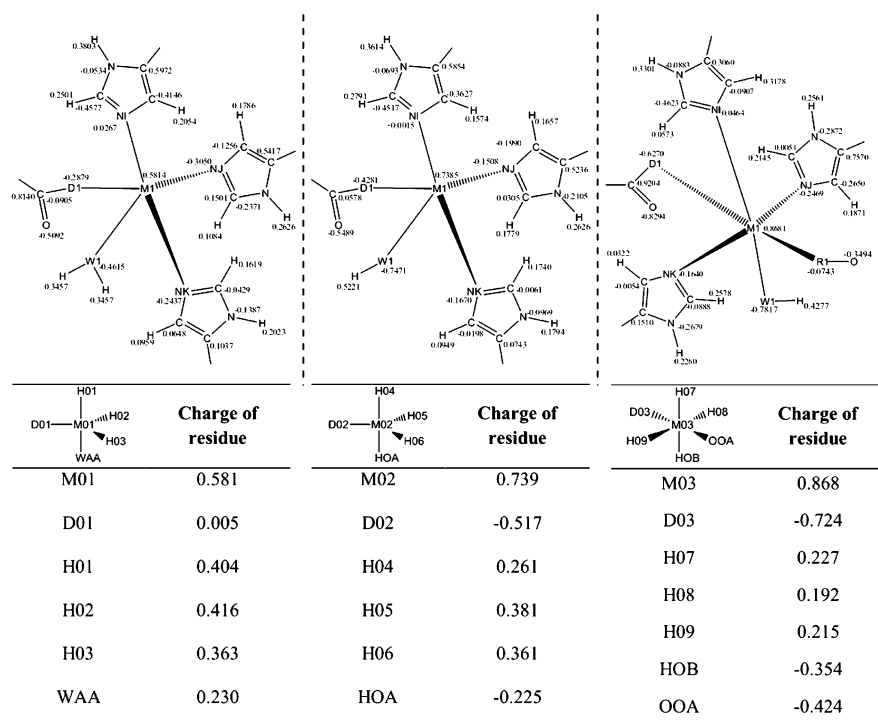


Figure 6. Representation of the single point Merz–Kollman charges fitted with the RESP methodology for three models concerning manganese superoxide dismutase with Mn^{3+} , and global charge of the residues for the three models derived from manganese superoxide dismutase. Charges are written in atomic units (a.u.).

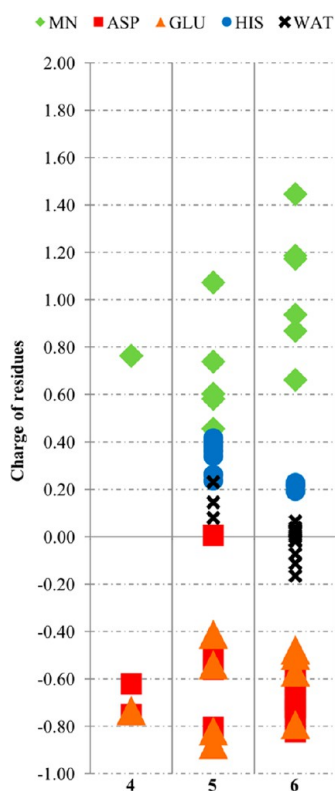


Figure 7. Global charge distribution for the main residues of the studied models, by residue and coordination number of the model.

coordination sphere. We employed MD and MM calculations to generate data populations and normal mode information for each of the 12 models.

The scaling factor for the 1–4 electrostatic interactions was defined for classical mechanics calculations in order to reproduce better the equilibrium geometries, determined by quantum calculations in vacuum (validation of the electrostatic scaling is supplied in the Supporting Information).

RMSd Values. The results for the RMSd of the models parametrized are shown below (RMSd for the protein backbone chain and the Mn centers are presented in the Supporting Information). Figure 8 shows the RMSd plots for 4 of the 12 parametrized metalcenters (models (4)–(7)) during the 10 ns MD simulation.

An initial overview shows that, in the majority of the models, the backbone stabilized within the first 6 ns of the MD simulation.

The RMSd values of the Mn centers parametrized are generally smaller than 1.25 Å and, as for the accumulated averages, are generally stabilized within the last 4 ns of MD. Therefore, we define this time range as the scope of our statistical analysis.

In Table 2, we present the RMSd averages and standard deviations from the last 4 ns of the MD simulations. RMSd values are higher than expected. However, we also observed significant differences between the crystallographic and the respective quantum optimized coordinates. The differences between the QM and MM model are generally smaller. Moreover, in a few cases, we exchanged the metal in the X-ray structure for Mn and, in those cases, differences between the bond length of the experimental and calculated structures are expected.

We emphasize, nonetheless, that crystallographic structures are estimations over electronic density determined maps and differ among them.^{89,90} Therefore, deviations from the simulations may be analyzed taking into account additional considerations, such as mechanistic information on the

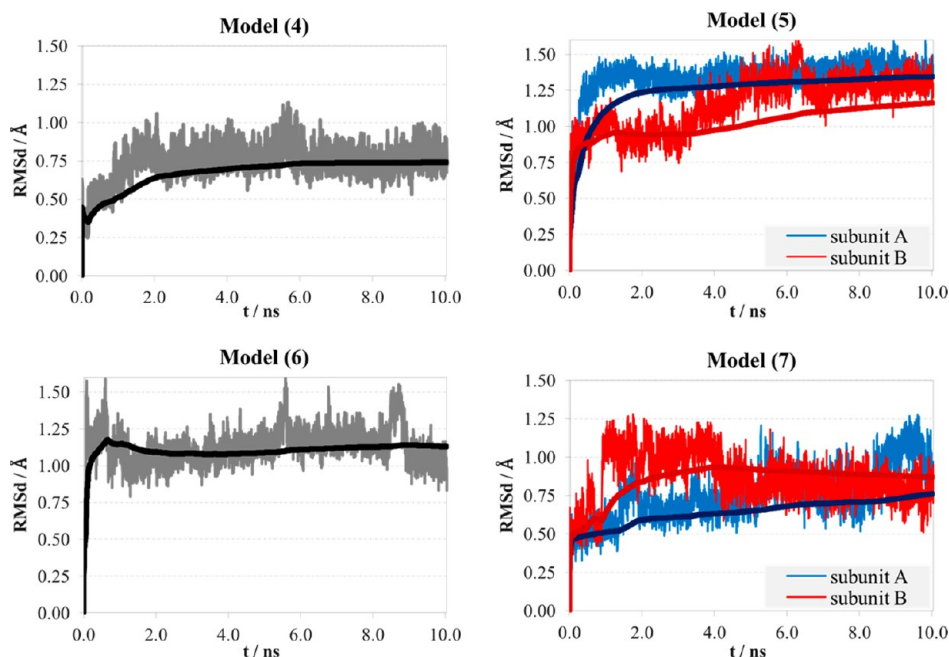


Figure 8. Graphs showing the root mean square deviations (RMSd) (thin lines) and the accumulated averages (thicker lines) for models (4)–(7), during the 10 ns of molecular dynamics (MD) simulation.

Table 2. RMSd Averages and Standard Deviations for the Proteins (Right Column) and the Small Models (Left Column)

code of the model	$\langle \text{RMSd} \rangle \pm \sigma_{\text{RMSd}} (\text{\AA})$	
	metallocenter	protein
HHDHW (III)	1.00 ± 0.09	3.3 ± 0.2
HHDH[HO] (III)	1.21 ± 0.09	2.7 ± 0.2
HHDH[HO]O (III)	0.41 ± 0.08	2.3 ± 0.2
HDEWWW (II)	0.76 ± 0.07	2.9 ± 0.1
DENWWW (II)	1.35 ± 0.09	3.5 ± 0.2
DDWWWW (II)	1.2 ± 0.1	2.9 ± 0.3
DEDWWW (II)	0.8 ± 0.1	2.2 ± 0.1
ED[PY2]WW (II)	0.6 ± 0.1	3.4 ± 0.3
HHEWW (II)	0.7 ± 0.2	1.9 ± 0.1
DEE[SO2] (II)	0.07 ± 0.02	1.6 ± 0.1
HHE[D2] (II)	0.41 ± 0.06	2.5 ± 0.1
DED[CL] (II)	0.47 ± 0.06	2.9 ± 0.1

coordination sphere of the metal ion, which allows further detail than the crystallographic structures alone.

Bond Stretching and Angle Bending Coordinates. The results of the bond lengths between the metal and its ligands, taken from the crystallographic structure (l_{crystal}), the quantum mechanical model (l_{opt}), and the average from the 4 ns MD population ($\langle l \rangle_{\text{MD}}$), are presented in the Supporting Information.

The standard deviations of the 4 ns bond length population are proximate to the maximum stretching scanned in the PES calculation. However, this has not been verified for most of the water ligands. Considering the range $\langle l \rangle_{\text{MD}} \pm \sigma_l$ for each of the bonds established, 82% of the optimized Mn–ligand bonds are included in the given range. For twice this range, 98% of the optimized bond equilibrium values parametrized are included in the given interval.

For the same given interval $\langle \theta \rangle_{\text{MD}} \pm \sigma_\theta$, only 66% of the parametrized angles fit in the range defined. However, the standard deviations determined are often $<5^\circ$, which is a low

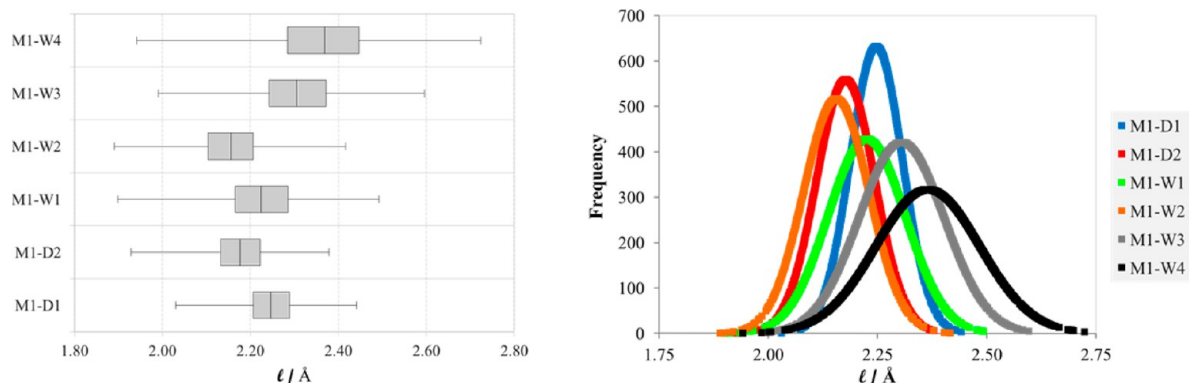


Figure 9. Distribution for the bonds of model (6) with quartile representation and Gaussian curve fitting, for the last 4 ns of the MD run. All the representations and further validation on the Gaussian fitting are given in the Supporting Information.

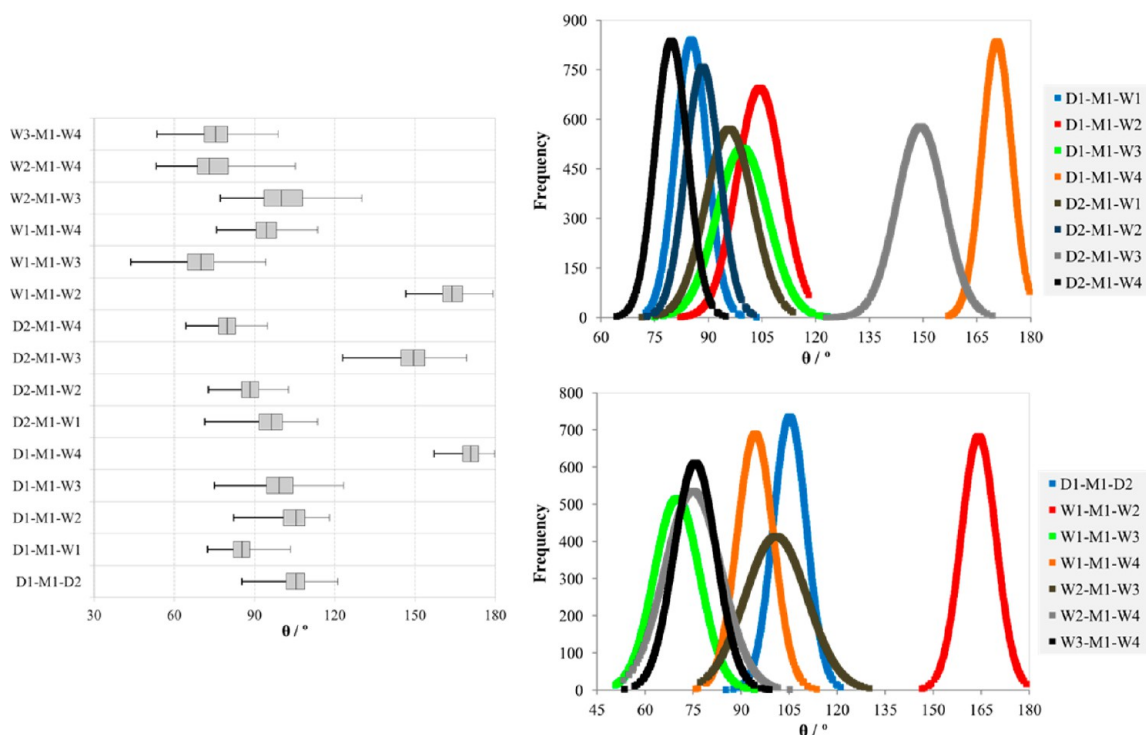


Figure 10. Distribution of the data for the angles in model (6) with quartile distribution and approaching a Gaussian curve, for the last 4 ns of the MD run, shown as an example. Other distribution data can be found in the Supporting Information.

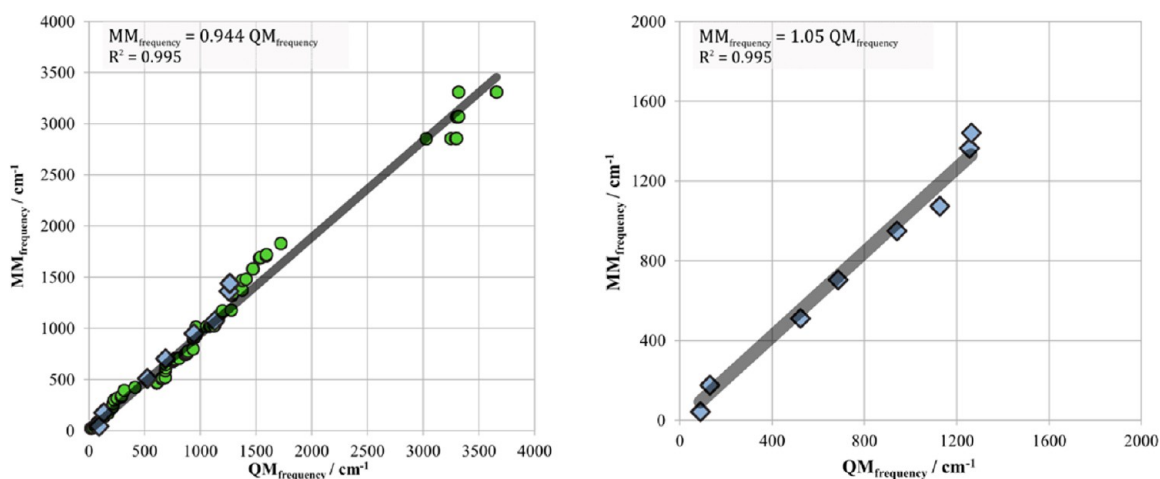


Figure 11. Comparison of vibrational frequencies for the model HHDH[HO] (III) optimized with the AMBER force field and at B3LYP/SDD:6-31G(d,p) level of theory (on the left) and normal modes involving the donor and acceptor atoms (on the right).

value if attending to the flatness of the PESs for these small force constants. For an error estimate of ~ 1 kcal mol $^{-1}$, an angle bending often higher than twice the standard deviation is required. Considering a new range $\langle \theta \rangle_{\text{MD}} \pm 2\sigma_{\theta}$, 89% of the optimized equilibrium angle bending values are included in the defined interval, for the determined force constants.

To analyze the information on the population studied, quartile and histogram distributions were produced. Quartile distributions allow a glimpse of the symmetry of the population and the range of the full sampling, while histogram/normal distributions allow further considerations on the flatness of the population and the comparison of the optimized and averaged values.

Figures 9 and 10 present the quartile distributions and normal curves for the bonds and angles involving the Mn atom

for model (6), as an example. Quartile and Gaussian distributions are presented in detail in the Supporting Information, as well as further validation of the Gaussian curve fitting.

A quartile distribution represents a distribution of the population in blocks of 25% of the data from the last 4 ns of MD simulation, in an increasing order. The first and last 25% of the population values (the first and fourth quartiles) are represented as the tails of the distribution, while the second and third quartiles are represented by boxes, divided by the central value of the population (the median value). From the quartile distribution, we can see the general range of the distribution and the concentration of the sampling around the median value.

The normal curve fitting, validated by the histogram representation, estimates the predominance of each single coordinate in the population.

To establish the histogram representation, data on the final 4 ns population was organized in intervals with a range close to the standard deviation values obtained (0.05 Å for bonds and 5° for angles).

Generally, quartile and histogram plots for both bond and angle coordinates show that the median and average values are close, thus supporting the average values determined. The ranges of the boxes around the median, from the quartile representation, point toward an apparent symmetry in the considered populations.

A more spread distribution of the bond length values can be observed for farther Mn–ligand distances. Even though only 69% of the optimized bond lengths are counted in the two quartiles around the median, these quartiles, however, are, on average, spread ~ 0.08 Å from the median.

From Figure 10, we observe that, for similar angle bending amplitudes, populations involving O–Mn–water and N–Mn–water interactions have larger standard deviations than the remaining interactions. The length of both boxes accounting for 50% of the population, around the median is, on average, $\sim 6^\circ$. However, the normal fitting curve shows that angle populations have flatter distributions than quartile plots might resemble. In Gaussian curves, it can be seen that, in most cases, for a range of 8° – 10° , only 67% of the angle population would be found around the average value. Since the average and median values are close, it means that, for an increase in range up to 4° , only an additional 17% of the population is included.

All the statistical validation seems to point toward good reliability in the parameters determined.

Frequency and Normal Mode Analysis. Comparison of the frequencies of the parametrized models and the original QM models shows that the parameters calculated reproduce the frequency profile expected from quantum mechanics calculations. Figure 11 shows a graphical comparison of the QM and MM vibrational frequencies for one of the parametrized models.

This, however, does not guarantee that normal modes for both models match. Particularly, it would be helpful to find equivalent normal modes in both models and compare their mass-weighted frequencies. Therefore, we show, for 4 of the 12 models (models HHDH[HO] (III), HDEWWW (II), HHE[D2] (II), and DED[CL] (II)), the correlation for MM vs QM frequencies, describing similar normal modes. We searched normal modes for which displacements of metal–ligand bonds were similar in QM and MM models.

We calculated first the RMSd between the MM optimized models and the QM optimized models (detailed plots follow in the Supporting Information). Large differences are registered in the backbone atoms and in the carboxylate oxygens not coordinated to the manganese center. Since the backbone atoms were not targeted by our parametrization scheme, we performed a RMSd calculation based on the heavy atoms of the organic ligands and side chains of bonded amino acids; as can be seen in Table 3, RMSd values for our parametrized models are smaller than 1.4 Å.

The differences between the bond lengths calculated in the QM and MM geometry optimizations ranged from 0.002 Å to 0.20 Å (average = 0.04 Å).

Correlations between the Parameters. Beyond the scope of the parameter determination, we expect our results

Table 3. RMSd for the Optimized Models from the Comparison of the QM and MM Optimized Structures

	RMSd (Å)	
	heavy atoms	heavy atoms not from backbone
HHDHW (III)	1.22	0.75
HHDH[HO] (III)	1.83	0.92
HHDH[HO]O (III)	1.92	1.07
HDEWWW (II)	0.90	0.51
DENWWW (II)	1.73	1.10
DDWWW (II)	1.55	0.50
DEDWWW (II)	1.82	0.98
ED[PY2]WW (II)	1.88	0.87
HHEWW (II)	1.61	1.18
DEE[SO2] (II)	1.92	1.06
HHE[D2] (II)	2.81	1.38
DED[CL] (II)	1.80	1.04

to lead to some estimates on parameter behavior in manganese-containing proteins. It is expected and desirable that the parameters would be transferable for systems with similar coordination spheres. Moreover, we also expect to provide estimates in force constants concerning typical donor atoms or geometrical dispositions in Mn-coordinated centers and, ultimately, save computational resources in future projects involving this class of proteins.

Figures 12 and 13 illustrate all the 65 bond force constants, taking into account the equilibrium bond lengths of the corresponding interactions. These are grouped by specific Mn–ligand type interaction (by residue) and donor atom (by element). Regarding bond force constants, linear and second-order polynomial regressions were performed to establish correlations for force constants and equilibrium bond lengths on ligands and donor atoms.

Waters are small, flexible, and distant ligands in their coordination with the metal center; therefore, they are difficult to predict. For the 18 bonds between the Mn ion and waters, a good sampling was obtained and an average correlation between bond force constants and bond lengths was established. Therefore, rough force constants can be estimated for any water in a given coordination sphere. Such correlation seems to be unrelated to the charge of the manganese center or the coordination.

We calculated correlations for the remaining frequent ligand amino acids; however, sampling is lower and generally have a wider distribution, particularly for aspartates and glutamates.

The linear regressions established seem to support similar bonding behaviors for aspartates and glutamates. Extending the fitting to large bond lengths, we should expect that the force constants converge to zero; therefore, force constants must be obtained by *interpolation* rather than *extrapolation*. A range of 2.00–2.30 Å and 2.00–2.20 Å is defined for the aspartate and glutamate bonds, respectively, whereas for histidine, an interval from 2.00 Å to 2.25 Å is suggested, and for water, an interval from 2.15 Å to 2.40 Å is suggested.

To estimate force constants for less-common ligands, the second-order polynomial regression plotted in Figure 13 can be used. Although good correlations for rough estimates have been attained, the estimated force constants can be affected by errors in the range of $17 \text{ kcal mol}^{-1} \text{ Å}^{-2}$ and $8 \text{ kcal mol}^{-1} \text{ Å}^{-2}$, respectively. Also, the graphical representations in Figures 12 and 13 seem to support the premise that coordination number does not affect the force constants significantly.

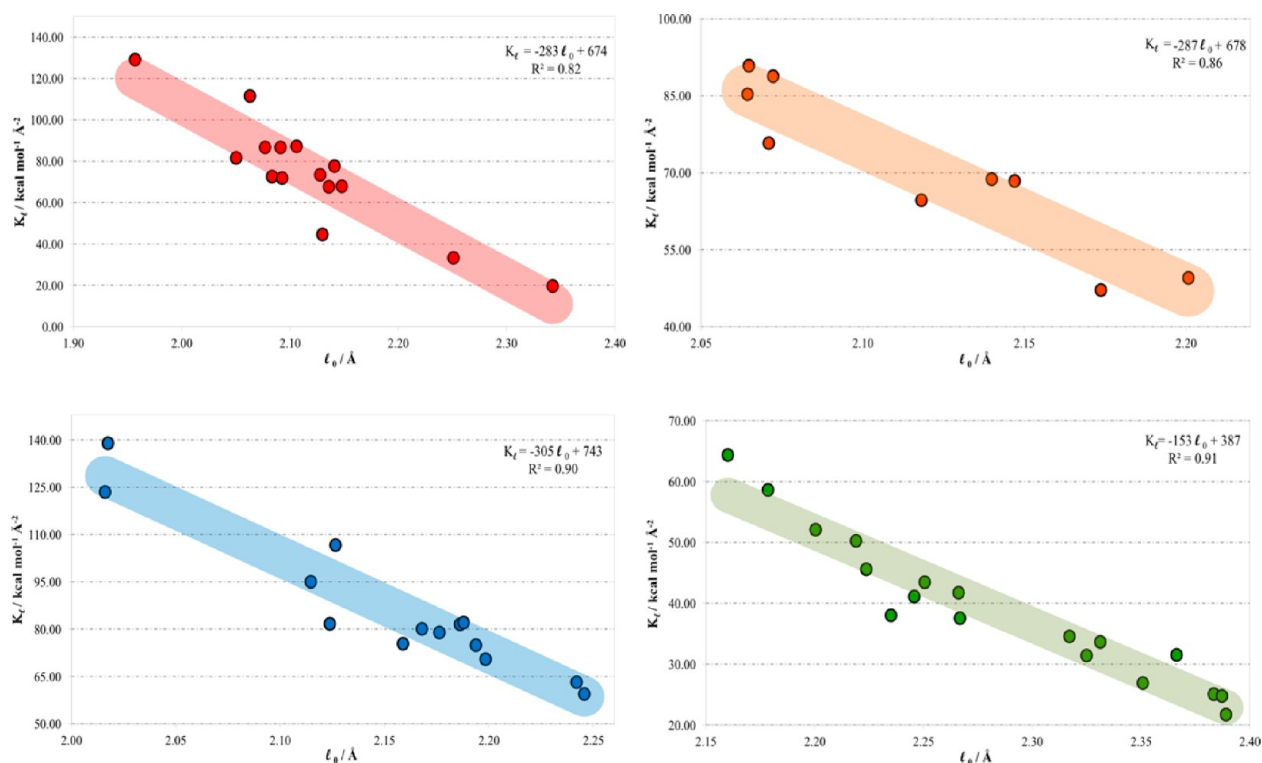


Figure 12. Linear regression for the main ligands in Mn-coordination spheres: aspartate, glutamate, histidine, and water, shown in red, orange, blue, and green, respectively.

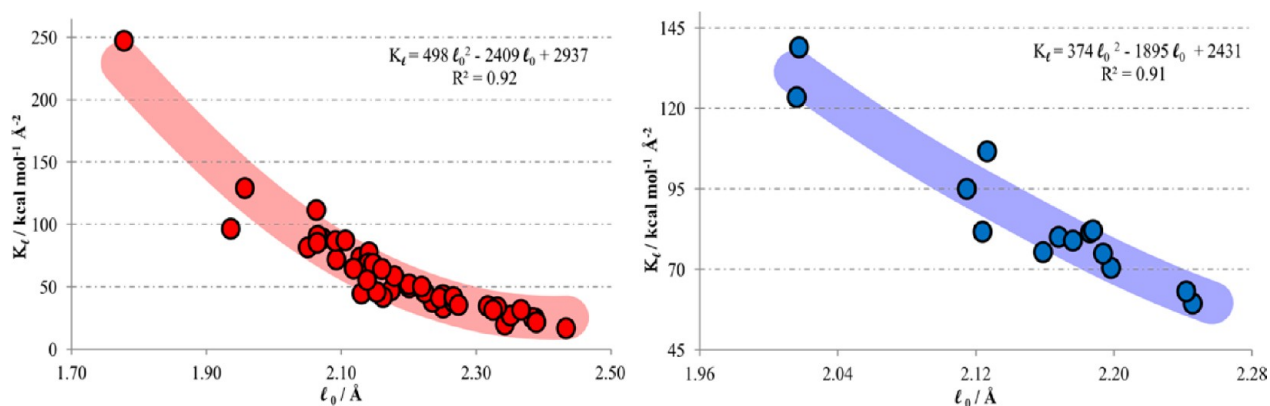


Figure 13. Second-order polynomial regression for the main donor atoms in Mn-coordination spheres (oxygen and nitrogen are shown in red and blue colors, respectively).

From the representation of the angle force constants versus angle equilibrium value, only dispersion patterns are observed. Angle force constants depend on bond lengths between donor atoms and the metal center and angle amplitude, meaning that a three-variable dependence representation, $K_\theta(\theta_0, l_{\text{Mn-L1}}, l_{\text{Mn-L2}})$, could allow for a more regular understanding of their behavior.

Although a clear pattern was not achieved by analysis of Mn-centered angle results, rough estimates are proposed in Table 4 and are shown in Figure 14 with the standard deviation assigned to it. The estimate that followed originated from the equilibrium coordinate for a given interaction in a range of $\sim 8^\circ$ from the equilibrium position from the nondistorted geometry, except for the axial positions, in which a 15° amplitude was considered (anticlockwise only).

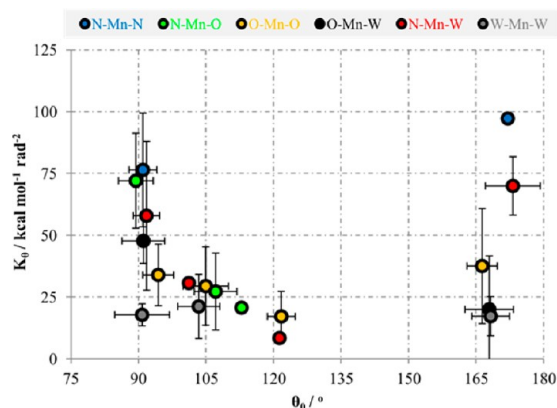
We can observe that angle force constants generally diminish as the average equilibrium amplitude increases; however, for the axial interaction of equal nonwater ligands, a slight increase in the force constant is verified. Also, large standard deviations are observed, independently of the sampling dimension considered, for the average force constants determined. Considering the maximum standard deviations observed in the MD simulations, maximum energy errors can reach 8 kcal mol^{-1} for angles involving water ligands or 3 kcal mol^{-1} for the remaining ligands.

CONCLUSIONS

We have determined bond, angle, and electrostatic parameters for a set of 12 semiflexible Mn-coordination spheres from 9 metalloproteins, following the philosophy of the AMBER force field.

Table 4. Estimate Values for the Equilibrium Angles in Frequent Manganese Coordination Geometries

angle	$\langle\theta_0\rangle \pm \sigma_{\theta_0}$	$\langle K_{\theta}\rangle \pm \sigma_{K_{\theta}}$	number of cases
N–Mn–N _{axial}	172.06	97	1
N–Mn–N _{equatorial 90°}	91 ± 3	(8 ± 2) × 10	6
N–Mn–N _{tetrahedral}	107 ± 1	35.0 ± 0.9	2
N–Mn–O _{equatorial 90°}	89 ± 4	(7 ± 2) × 10	9
N–Mn–O _{equatorial 120°}	113	21	1
N–Mn–O _{tetrahedral}	107 ± 5	(3 ± 2) × 10	6
O–Mn–O _{axial}	166 ± 3	(4 ± 2) × 10	5
O–Mn–O _{equatorial 90°}	94 ± 3	(3 ± 1) × 10	10
O–Mn–O _{equatorial 120°}	122 ± 3	(2 ± 1) × 10	6
O–Mn–O _{tetrahedral}	105 ± 5	(3 ± 2) × 10	8
O–Mn–W _{axial}	168 ± 5	20 ± 7	3
O–Mn–W _{equatorial 90°}	91 ± 5	(5 ± 2) × 10	23
O–Mn–W _{tetrahedral}	104 ± 4	27 ± 9	5
N–Mn–W _{axial}	173 ± 6	(7 ± 1) × 10	3
N–Mn–W _{equatorial 90°}	92 ± 3	(6 ± 3) × 10	10
N–Mn–W _{equatorial 120°}	121	8	1
N–Mn–W _{tetrahedral}	101	31	1
W–Mn–W _{axial}	168 ± 4	17 ± 8	2
W–Mn–W _{equatorial 90°}	91 ± 6	18 ± 5	8
W–Mn–W _{tetrahedral}	103 ± 5	(2 ± 1) × 10	2

**Figure 14.** Average equilibrium angles and force constants for main donor atoms concerning the equilibrium angles for the main geometries in manganese.

The determined parameters include bond stretching and angle bending force constants, and their equilibrium values, as well as the RESP charges for all the residues in each of the coordination spheres. We have calculated 65 bond force constants, 146 angle force constants, and 12 RESP map charges, from a total of 74 residues, for the Mn centers chosen from the literature.

Validation of the determined parameters was carried out by analysis of molecular dynamics (MD) simulations on the metalloproteins chosen in the literature and an analysis of Mn-involving bond and angle parameters from stable metalloproteins was obtained from averaged values and statistical distributions (quartile, histogram, and Gaussian distributions), highlighting some important aspects in the behavior of the coordination sphere. Typical bond stretching and angle bending values were observed and confidence intervals were established to compare average values with those obtained from the quantum optimizations of the parametrized models. Approximately symmetrical populations were observed for both evaluated coordinates.

In addition, we propose correlations taking into consideration the atom type and typical ligands in Mn centers; therefore, other Mn centers in biology can be targeted using the bonded model approach. Linear correlations were established to estimate bond force constants for typical residues in Mn centers. Higher-order correlations were proposed in order to estimate rough bond force constants, given typical donor atoms. Angle bending interactions were evaluated by analysis of an obtained dispersion pattern. Some estimates were proposed for the main positions exhibited by Mn centers: axial, quadrangular planar, triangular planar, and tetrahedral.

The important results obtained so far strongly support that recurrence can be found in other metalloproteic systems. The established parameters will allow for future relevant mechanistic and catalytic insight on the manganese proteins.

■ ASSOCIATED CONTENT

● Supporting Information

Description of the nomenclature defined to identify coordinating residues and the donor/acceptor atoms. Detailed description of the considerations and literature support for the optimization procedure for each model. Tables with detailed information on the Mn-ligand bond and angle force constants and equilibrium coordinates. Charge mapping for the 12 models used for parametrization. Validation procedure of the 1–4 electrostatic factor applied for MD simulations. RMSd plots of the backbone and metalcenter for the 10 ns MD simulations applied in each structure containing the metallocenter. Detailed tables comparing crystallographic, optimized, and average equilibrium Mn-ligand bond and angle values. Quartile and Gaussian distributions for the 12 metalloenzymes simulated. Histogram distribution and Gaussian curve approximation validation for the 12 simulated metalloenzymes. Frequency calculations at the MM and QM levels of theory for the 12 parametrized models and normal modes analysis on 4 of the parametrized models. Internal coordinate analysis for the donating and acceptor atoms and atomic fluctuations on heavy atoms from the optimizations at the MM and QM levels of theory. This material is available free of charge via the Internet at <http://pubs.acs.org>.

■ AUTHOR INFORMATION

Corresponding Author

*E-mail: mjramos@fc.up.pt.

Notes

The authors declare no competing financial interest.

■ ACKNOWLEDGMENTS

We thank the financial support provided by Fundação para a Ciência e Tecnologia (Project Nos. SFRH/BD/78397/201 and PTDC/QUI-QUI/103118/2008 and Grant No. Pest-C/EQB/LA0006/2011).

■ REFERENCES

- (1) Comba, P.; Hambley, T. W.; Stroble, M. The directionality of d-orbitals and molecular-mechanics calculations of octahedral transition-metal compounds. *Helv. Chim. Acta* **1995**, *78*, 2042–2047.
- (2) Banci, L. Molecular dynamics simulations of metalloproteins. *Curr. Opin. Chem. Biol.* **2003**, *7*, 143–149.
- (3) Hu, L. H.; Ryde, U. Comparison of Methods to Obtain Force-Field Parameters for Metal Sites. *J. Chem. Theory Comput.* **2011**, *7*, 2452–2463.

- (4) Zhang, S. T.; Yan, H.; Wei, M.; Evans, D. G.; Duan, X. Valence Force Field for Layered Double Hydroxide Materials Based on the Parameterization of Octahedrally Coordinated Metal Cations. *J. Phys. Chem. C* **2012**, *116*, 3421–3431.
- (5) Seebeck, B.; Reulecke, I.; Kamper, A.; Rarey, M. Modeling of metal interaction geometries for protein–ligand docking. *Proteins* **2008**, *71*, 1237–1254.
- (6) Harding, M. M.; Nowicki, M. W.; Walkinshaw, M. D. Metals in protein structures: A review of their principal features. *Crystallogr. Rev* **2010**, *16*, 247–302.
- (7) Tafipolsky, M.; Amirjalayer, S.; Schmid, R. Ab initio parametrized MM3 force field for the metal-organic framework MOF-5. *J. Comput. Chem.* **2007**, *28*, 1169–1176.
- (8) Tamames, J. A. C.; Ramos, M. J. Metals in proteins: Cluster analysis studies. *J. Mol. Model.* **2011**, *17*, 429–442.
- (9) Berman, H. M.; Westbrook, J.; Feng, Z.; Gilliland, G.; Bhat, T. N.; Weissig, H.; Shindyalov, I. N.; Bourne, P. E. The Protein Data Bank. *Nucleic Acids Res.* **2000**, *28*, 235–242.
- (10) Weatherburn, D. C. Manganese-containing Enzymes and Proteins. In *Handbook on Metalloproteins*; Bertini, I., Siegel, A., Sigel, H., Eds.; Marcel Dekker: New York, 2001; Chapter 8, pp 193–268.
- (11) da Silva, J. J. R. F.; Williams, R. J. P. *The Biological Chemistry of the Elements: The Inorganic Chemistry of Life*. 2nd Edition; Oxford University Press: New York, 2001; p 600.
- (12) Siegbahn, P. E. M. Quantum chemical studies of manganese centers in biology. *Curr. Opin. Chem. Biol.* **2002**, *6*, 227–235.
- (13) Yocum, C. F.; Pecoraro, V. L. Recent advances in the understanding of the biological chemistry of manganese. *Curr. Opin. Chem. Biol.* **1999**, *3*, 182–187.
- (14) Stich, T. A.; Lahiri, S.; Yeagle, G.; Dicus, M.; Brynda, M.; Gunn, A.; Aznar, C.; DeRose, V. J.; Britt, R. D. Multifrequency pulsed EPR studies of biologically relevant manganese(II) complexes. *Appl. Magn. Reson.* **2007**, *31*, 321–341.
- (15) Sousa, S. F.; Fernandes, P. A.; Ramos, M. J. Molecular Dynamics Simulations: Difficulties, Solutions and Strategies for Treating Metalloenzymes. In *Kinetics and Dynamics: From Nano- to Bio-Scale*; Paneth, P., Dybala-Defratyka, A., Eds.; Springer: Dordrecht, The Netherlands: 2010; Chapter 11, pp 299–330.
- (16) Stote, R. H.; Karplus, M. Zinc binding in proteins and solution: A simple but accurate nonbonded representation. *Proteins* **1995**, *23*, 12–31.
- (17) Pang, Y. P.; Xu, K.; El Yazal, J.; Prendergast, F. G. Successful molecular dynamics simulation of the zinc-bound farnesyltransferase using the cationic dummy atom approach. *Protein Sci.* **2000**, *9*, 1857–1865.
- (18) Hoops, S. C.; Anderson, K. W.; Merz, K. M. Force field design for metalloproteins. *J. Am. Chem. Soc.* **1991**, *113*, 8262–8270.
- (19) Donini, O. A. T.; Kollman, P. A. Calculation and prediction of binding free energies for the matrix metalloproteinases. *J. Med. Chem.* **2000**, *43*, 4180–4188.
- (20) Dal Peraro, M. D.; Spiegel, K.; Lamoureux, G.; De Vivo, M.; DeGrado, W. F.; Klein, M. L. Modeling the charge distribution at metal sites in proteins for molecular dynamics simulations. *J. Struct. Biol.* **2007**, *157*, 444–453.
- (21) Wu, R.; Lu, Z.; Cao, Z.; Zhang, Y. A Transferable Nonbonded Pairwise Force Field to Model Zinc Interactions in Metalloproteins. *J. Chem. Theory Comput.* **2011**, *7*, 433–443.
- (22) Sousa, S. F.; Fernandes, P. A.; Ramos, M. J. The carboxylate shift in zinc enzymes: A computational study. *J. Am. Chem. Soc.* **2007**, *129*, 1378–1385.
- (23) Marcial, B. L.; Sousa, S. F.; Barbosa, I. L.; Dos Santos, H. F.; Ramos, M. J. Chemically Modified Tetracyclines as Inhibitors of MMP-2 Matrix Metalloproteinase: A Molecular and Structural Study. *J. Phys. Chem. B* **2012**, *116*, 13644–13654.
- (24) Lee, C. W.; Chakravorty, D. K.; Chang, F. M. J.; Reyes-Caballero, H.; Ye, Y. Z.; Merz, K. M.; Giedroc, D. P. Solution Structure of Mycobacterium tuberculosis NmtR in the Apo State: Insights into Ni(II)-Mediated Allostery. *Biochemistry* **2012**, *51*, 2619–2629.
- (25) Hu, L. H.; Farrokhnia, M.; Heimdal, J.; Shleev, S.; Rulisek, L.; Ryde, U. Reorganization Energy for Internal Electron Transfer in Multicopper Oxidases. *J. Phys. Chem. B* **2011**, *115*, 13111–13126.
- (26) Sindhikara, D. J.; Roitberg, A. E.; Merz, K. M. Apo and Nickel-Bound Forms of the Pyrococcus horikoshii Species of the Metalloregulatory Protein: NikR Characterized by Molecular Dynamics Simulations. *Biochemistry* **2009**, *48*, 12024–12033.
- (27) Shahrokhi, K.; Orendt, A.; Yost, G. S.; Cheatham, T. E., III Quantum Mechanically Derived AMBER-Compatible Heme Parameters for Various States of the Cytochrome P450 Catalytic Cycle. *J. Comput. Chem.* **2012**, *33*, 119–133.
- (28) Norrby, P. O.; Brandt, P. Deriving force field parameters for coordination complexes. *Coord. Chem. Rev.* **2001**, *212*, 79–109.
- (29) Cornell, W. D.; Cieplak, P.; Bayly, C. I.; Gould, I. R.; Merz, K. M.; Ferguson, D. M.; Spellmeyer, D. C.; Fox, T.; Caldwell, J. W.; Kollman, P. A. 2nd Generation Force-Field for the Simulation of Proteins, Nucleic-Acids, and Organic Molecules. *J. Am. Chem. Soc.* **1995**, *117*, 5179–5197.
- (30) Mackerell, A. D.; Wiorkiewiczkuczera, J.; Karplus, M. An all-atom empirical energy function for the simulation of nucleic acids. *J. Am. Chem. Soc.* **1995**, *117*, 11946–11975.
- (31) MacKerell, A. D.; Bashford, D.; Bellott, M.; Dunbrack, R. L.; Evanseck, J. D.; Field, M. J.; Fischer, S.; Gao, J.; Guo, H.; Ha, S.; Joseph-McCarthy, D.; Kuchnir, L.; Kucera, K.; Lau, F. T. K.; Mattos, C.; Michnick, S.; Ngo, T.; Nguyen, D. T.; Prodhom, B.; Reiher, W. E.; Roux, B.; Schlenkerich, M.; Smith, J. C.; Stote, R.; Straub, J.; Watanabe, M.; Wiorkiewicz-Kuczera, J.; Yin, D.; Karplus, M. All-atom empirical potential for molecular modeling and dynamics studies of proteins. *J. Phys. Chem. B* **1998**, *102*, 3586–3616.
- (32) Pranata, J.; Wierschke, S. G.; Jorgensen, W. L. OPLS potential functions for nucleotide bases. Relative association constants of hydrogen-bonded base pairs in chloroform. *J. Am. Chem. Soc.* **1991**, *113*, 2810–2819.
- (33) Damm, W.; Frontera, A.; Tirado-Rives, J.; Jorgensen, W. L. OPLS all-atom force field for carbohydrates. *J. Comput. Chem.* **1997**, *18*, 1955–1970.
- (34) Kaminski, G. A.; Friesner, R. A.; Tirado-Rives, J.; Jorgensen, W. L. Evaluation and reparametrization of the OPLS-AA force field for proteins via comparison with accurate quantum chemical calculations on peptides. *J. Phys. Chem. B* **2001**, *105*, 6474–6487.
- (35) Mackerell, A. D. Empirical force fields for biological macromolecules: Overview and issues. *J. Comput. Chem.* **2004**, *25*, 1584–1604.
- (36) Peters, M. B.; Yang, Y.; Wang, B.; Fusti-Molnar, L.; Weaver, M. N.; Merz, K. M. Structural Survey of Zinc-Containing Proteins and Development of the Zinc AMBER Force Field (ZAFF). *J. Chem. Theory Comput.* **2010**, *6*, 2935–2947.
- (37) Sousa, S. F.; Fernandes, P. A.; Ramos, M. J. Effective tailor-made force field parameterization of the several Zn coordination environments in the puzzling FTase enzyme: Opening the door to the full understanding of its elusive catalytic mechanism. *Theor. Chem. Acc.* **2007**, *117*, 171–181.
- (38) Comba, P.; Remenyi, R. Inorganic and bioinorganic molecular mechanics modeling—The problem of the force field parameterization. *Coord. Chem. Rev.* **2003**, *238*, 9–20.
- (39) Lin, F.; Wang, R. X. Systematic Derivation of AMBER Force Field Parameters Applicable to Zinc-Containing Systems. *J. Chem. Theory Comput.* **2010**, *6*, 1852–1870.
- (40) Borgstahl, G. E. O.; Parge, H. E.; Hickey, M. J.; Beyer, W. F.; Hallewell, R. A.; Tainer, J. A. The structure of human mitochondrial manganese superoxide dismutase reveals a novel tetrameric interface of two 4-helix bundles. *Cell* **1992**, *71*, 107–118.
- (41) Lah, M. S.; Dixon, M. M.; Patridge, K. A.; Stallings, W. C.; Fee, J. A.; Ludwig, M. L. Structure-function in Escherichia coli iron superoxide dismutase: Comparisons with the manganese enzyme from Thermus thermophilus. *Biochemistry* **1995**, *34*, 1646–1660.
- (42) Koepke, J.; Olkhova, E.; Angerer, H.; Mueller, H.; Peng, G.; Michel, H. High resolution crystal structure of *Paracoccus denitrificans*

Cytochrome C oxidase: New insights into the active site and the proton transfer pathways. *Biochim. Biophys. Acta* **2009**, *1787*, 635–645.

(43) Fedorov, A. A.; Fedorov, E. V.; Gerlt, J. A.; Burley, S. K.; Almo, S. C. Crystal structure of Glucarate dehydratase from *Burkholderia cepacia* complexed with magnesium. (*To be Published*) **2010**.

(44) Lubkowski, J.; Yang, F.; Alexandratos, J.; Wlodawer, A.; Zhao, H.; Burke, T. R.; Neamati, N.; Pommier, Y.; Merkel, G.; Skalka, A. M. Structure of the catalytic domain of avian sarcoma virus integrase with a bound HIV-1 integrase-targeted inhibitor. *Proc. Natl. Acad. Sci. U.S.A.* **1998**, *95*, 4831–4836.

(45) Sakai, A.; Fedorov, A. A.; Fedorov, E. V.; Schnoes, A. M.; Glasner, M. E.; Brown, S.; Rutter, M. E.; Bain, K.; Chang, S.; Gheyi, T.; Sauder, J. M.; Burley, S. K.; Babbitt, P. C.; Almo, S. C.; Gerlt, J. A. Evolution of Enzymatic Activities in the Enolase Superfamily: Stereochemically Distinct Mechanisms in Two Families of cis,cis-Muconate Lactonizing Enzymes. *Biochemistry* **2009**, *48*, 1445–1453.

(46) Williams, R.; Holyoak, T.; McDonald, G.; Gui, C.; Fenton, A. W. Differentiating a ligand's chemical requirements for allosteric interactions from those for protein binding. Phenylalanine inhibition of pyruvate kinase. *Biochemistry* **2006**, *45*, 5421–5429.

(47) Vetting, M. W.; Wackett, L. P.; Que, L.; Lipscomb, J. D.; Ohlendorf, D. H. Crystallographic comparison of manganese- and iron-dependent homoprotocatechuate 2,3-dioxygenases. *J. Bacteriol.* **2004**, *186*, 1945–1958.

(48) Neidhart, D. J.; Howell, P. L.; Petsko, G. A.; Powers, V. M.; Li, R. S.; Kenyon, G. L.; Gerlt, J. A. Mechanism of the reaction catalyzed by mandelate racemase. 2. Crystal structure of mandelate racemase at 2.5-Å resolution: identification of the active site and possible catalytic residues. *Biochemistry* **1991**, *30*, 9264–9273.

(49) Lawrence, M. C.; Pilling, P. A.; Epa, V. C.; Berry, A. M.; Ogunniyi, A. D.; Paton, J. C. The crystal structure of pneumococcal surface antigen PsaA reveals a metal-binding site and a novel structure for a putative ABC-type binding protein. *Structure* **1998**, *6*, 1553–1561.

(50) Kleywegt, G. J.; Hoier, H.; Jones, T. A. A re-evaluation of the crystal structure of chloromuconate cycloisomerase. *Acta Crystallogr. D Biol. Crystallogr.* **1996**, *52*, 858–863.

(51) Carrasco, R.; Morgenstern-Badarau, I.; Cano, J. Two proton-one electron coupled transfer in iron and manganese superoxide dismutases: A density functional study. *Inorg. Chim. Acta* **2007**, *360*, 91–101.

(52) Srncic, M.; Aquilante, F.; Ryde, U.; Rulisek, L. Reaction Mechanism of Manganese Superoxide Dismutase Studied by Combined Quantum and Molecular Mechanical Calculations and Multiconfigurational Methods. *J. Phys. Chem. B* **2009**, *113*, 6074–6086.

(53) Georgiev, V.; Borowski, T.; Siegbahn, P. E. M. Theoretical study of the catalytic reaction mechanism of MndD. *J. Biol. Inorg. Chem.* **2006**, *11*, 571–585.

(54) Michel, H.; Behr, J.; Harrenga, A.; Kannt, A. Cytochrome C oxidase: Structure and spectroscopy. *Annu. Rev. Biophys. Biomol. Struct.* **1998**, *27*, 329–356.

(55) Wooll, J. O.; Friesen, R. H. E.; White, M. A.; Watowich, S. J.; Fox, R. O.; Lee, J. C.; Czerwinski, E. W. Structural and functional linkages between subunit interfaces in mammalian pyruvate kinase. *J. Mol. Biol.* **2001**, *312*, 525–540.

(56) Frisch, M. J.; Trucks, G. W.; Schlegel, H. B.; Scuseria, G. E.; Robb, M. A.; Cheeseman, J. R.; Scalmani, G.; Barone, V.; Mennucci, B.; Petersson, G. A.; Nakatsuji, H.; Caricato, M.; Li, X.; Hratchian, H. P.; Izmaylov, A. F.; Bloino, J.; Zheng, G.; Sonnenberg, J. L.; Hada, M.; Ehara, M.; Toyota, K.; Fukuda, R.; Hasegawa, J.; Ishida, M.; Nakajima, T.; Honda, Y.; Kitao, O.; Nakai, H.; Vreven, T.; J. A. Montgomery, J.; Peralta, J. E.; Ogliaro, F.; Bearpark, M.; Heyd, J. J.; Brothers, E.; Kudin, K. N.; Staroverov, V. N.; Kobayashi, R.; Normand, J.; Raghavachari, K.; Rendell, A.; Burant, J. C.; Iyengar, S. S.; Tomasi, J.; Cossi, M.; Rega, N.; Millam, J. M.; Klene, M.; Knox, J. E.; Cross, J. B.; Bakken, V.; Adamo, C.; Jaramillo, J.; Gomperts, R.; Stratmann, R. E.; Yazyev, O.; Austin, A. J.; Cammi, R.; Pomelli, C.; Ochterski, J. W.; Martin, R. L.; Morokuma, K.; Zakrzewski, V. G.; Voth, G. A.; Salvador, P.;

Dannenberg, J. J.; Dapprich, S.; Daniels, A. D.; Farkas, Ö.; Foresman, J. B.; Ortiz, J. V.; Cioslowski, J.; Fox, D. J. *Gaussian 09, Revision A.1*, Gaussian, Inc.: Wallingford, CT, 2009.

(57) Becke, A. D. Density-functional exchange-energy approximation with correct asymptotic behavior. *Phys. Rev. A* **1988**, *38*, 3098–3100.

(58) Becke, A. D. Density-functional thermochemistry. 4. A new dynamical correlation functional and implications for exact-exchange mixing. *J. Chem. Phys.* **1996**, *104*, 1040–1046.

(59) Lee, C. T.; Yang, W. T.; Parr, R. G. Development of the Colle-Salvetti correlation-energy formula into a functional of the electron density. *Phys. Rev. B* **1988**, *37*, 785–789.

(60) Sousa, S. F.; Fernandes, P. A.; Ramos, M. J. General performance of density functionals. *J. Phys. Chem. A* **2007**, *111*, 10439–10452.

(61) Burke, K. Perspective on density functional theory. *J. Chem. Phys.* **2012**, *136*, 150901–150909.

(62) Blomberg, M. R. A.; Siegbahn, P. E. M. A quantum chemical approach to the study of reaction mechanisms of redox-active metalloenzymes. *J. Phys. Chem. B* **2001**, *105*, 9375–9386.

(63) Comba, P.; Remenyi, R. A new molecular mechanics force field for the oxidized form of blue copper proteins. *J. Comput. Chem.* **2002**, *23*, 697–705.

(64) Dunning, T. H., Jr.; Hay, P. J. In *Modern Theoretical Chemistry*, Schaefer, H. F., III, Ed.; Plenum Press: New York, 1976; Vol. 3, pp 1–28.

(65) Dolg, M.; Wedig, U.; Stoll, H.; Preuss, H. Energy-adjusted ab initio pseudopotentials for the first row transition elements. *J. Chem. Phys.* **1987**, *86*, 866–872.

(66) Ruth, K.; Tullmann, S.; Vitze, H.; Bolte, M.; Lerner, H. W.; Holthausen, M. C.; Wagner, M. Copper complexes of mono- and ditopic (methylthio)methyl borates: Missing links and linked systems en route to copper enzyme models. *Chemistry* **2008**, *14*, 6754–6770.

(67) Waller, M. P.; Braun, H.; Hojdis, N.; Buhl, M. Geometries of second-row transition-metal complexes from density-functional theory. *J. Chem. Theory Comput.* **2007**, *3*, 2234–2242.

(68) Yoshikai, N.; Zhang, S. L.; Yamagata, K.; Tsuji, H.; Nakamura, E. Mechanistic Study of the Manganese-Catalyzed 2 + 2+2 Annulation of 1,3-Dicarbonyl Compounds and Terminal Alkynes. *J. Am. Chem. Soc.* **2009**, *131*, 4099–4109.

(69) Sousa, S. F.; Carvalho, E. S.; Ferreira, D. M.; Tavares, I. S.; Fernandes, P. A.; Ramos, M. J.; Gomes, J. A. N. F. Comparative Analysis of the Performance of Commonly Available Density Functionals in the Determination of Geometrical Parameters for Zinc Complexes. *J. Comput. Chem.* **2009**, *30*, 2752–2763.

(70) Bayly, C. I.; Cieplak, P.; Cornell, W. D.; Kollman, P. A. A well-behaved electrostatic potential based method using charge restraints for deriving atomic charges: The RESP model. *J. Phys. Chem.* **1993**, *97*, 10269–10280.

(71) Suarez, D.; Brothers, E. N.; Merz, K. M. Insights into the structure and dynamics of the dinuclear zinc beta-lactamase site from *Bacteroides fragilis*. *Biochemistry* **2002**, *41*, 6615–6630.

(72) Yao, L. S.; Sklenak, S.; Yan, H. G.; Cukier, R. I. A molecular dynamics exploration of the catalytic mechanism of yeast cytosine deaminase. *J. Phys. Chem. B* **2005**, *109*, 7500–7510.

(73) Johansson, M. P.; Kaila, V. R. I.; Laakkonen, L. Charge parameterization of the metal centers in Cytochrome C oxidase. *J. Comput. Chem.* **2008**, *29*, 753–767.

(74) Smith, D. M. A.; Xiong, Y. J.; Straatsma, T. P.; Rosso, K. M.; Squier, T. C. Force-Field Development and Molecular Dynamics of NiFe Hydrogenase. *J. Chem. Theory Comput.* **2012**, *8*, 2103–2114.

(75) Sigfridsson, E.; Ryde, U. Comparison of methods for deriving atomic charges from the electrostatic potential and moments. *J. Comput. Chem.* **1998**, *19*, 377–395.

(76) Wang, J. M.; Cieplak, P.; Kollman, P. A. How well does a restrained electrostatic potential (RESP) model perform in calculating conformational energies of organic and biological molecules? *J. Comput. Chem.* **2000**, *21*, 1049–1074.

(77) Babu, C. S.; Lim, C. Empirical force fields for biologically active divalent metal cations in water. *J. Phys. Chem. A* **2006**, *110*, 691–699.

- (78) Merz, K. M.; Banci, L. Binding of bicarbonate to human carbonic anhydrase II: A continuum of binding states. *J. Am. Chem. Soc.* **1997**, *119*, 863–871.
- (79) Comba, P.; Hambley, T. W. *Molecular Modeling of Inorganic Compounds*; Wiley: Weinheim, Germany, 2008.
- (80) Case, D. A.; Darden, T. A.; T.E. Cheatham, I.; Simmerling, C. L.; Wang, J.; Duke, R. E.; Luo, R.; Crowley, M.; Walker, R. C.; Zhang, W.; Merz, K. M.; Wang, B.; Hayik, S.; Roitberg, A.; Seabra, G.; Kolossváry, I.; Wong, K. F.; Paesani, F.; Vanicek, J.; Wu, X.; Brozell, S. R.; Steinbrecher, T.; Gohlke, H.; Yang, L.; Tan, C.; Mongan, J.; Hornak, V.; Cui, G.; Mathews, D. H.; Seetin, M. G.; Sagui, C.; Babin, V.; Kollman, P. A. *AMBER 10*; University of California: San Francisco, 2008.
- (81) Wang, J.; Wang, W.; Kollman, P. A.; Case, D. A. Automatic atom type and bond type perception in molecular mechanical calculations. *J. Mol. Graph. Modell.* **2006**, *25*, 247–260.
- (82) Wang, J. M.; Wolf, R. M.; Caldwell, J. W.; Kollman, P. A.; Case, D. A. Development and testing of a general amber force field. *J. Comput. Chem.* **2004**, *25*, 1157–1174.
- (83) Jorgensen, W. L.; Chandrasekhar, J.; Madura, J. D.; Impey, R. W.; Klein, M. L. Comparison of simple potential functions for simulating liquid water. *J. Chem. Phys.* **1983**, *79*, 926–935.
- (84) van der Spoel, D.; van Maaren, P. J. The origin of layer structure artifacts in simulations of liquid water. *J. Chem. Theory Comput.* **2006**, *2*, 1–11.
- (85) Ewald, P. P. The calculation of optical and electrostatic grid potential. *Ann. Phys.–Berlin* **1921**, *64*, 253–287.
- (86) Ryckaert, J. P.; Ciccotti, G.; Berendsen, H. J. C. Numerical Integration of the Cartesian Equations of Motion of a System with Constraints: Molecular Dynamics of *n*-Alkanes. *J. Comput. Phys.* **1977**, *23*, 327–341.
- (87) Rulisek, L.; Ryde, U. Structure of reduced and oxidized manganese superoxide dismutase: A combined computational and experimental approach. *J. Phys. Chem. B* **2006**, *110*, 11511–11518.
- (88) Maciel, G. S.; Garcia, E. Study of charges transferability for use in force fields. *Chem. Phys. Lett.* **2006**, *420*, 497–502.
- (89) Harding, M. M. The geometry of metal–ligand interactions relevant to proteins. *Acta Crystallogr., Sect. D: Biol. Crystallogr.* **1999**, *55*, 1432–1443.
- (90) Harding, M. M. The geometry of metal–ligand interactions relevant to proteins. II. Angles at the metal atom, additional weak metal–donor interactions. *Acta Crystallogr., Sect. D: Biol. Crystallogr.* **2000**, *56*, 857–867.